Two-dimensional numerical simulation of water entry of a cylinder into waves using OpenFOAM

Kai Wang[1], Xin Ma[1]*, Wei Bai[2], Ling Qian[2], Zhi Li[1], Yibin Li[1]

[1]School of Control Science and Engineering, Shandong University, Shandong, CHINA

[2]Centre for Mathematical Modelling and Flow Analysis, School of Computing, Mathematics and Digital Technology, Manchester Metropolitan University, Manchester, M1 5GD, United Kingdom

*This work was supported by the Key Research and Development Project of Shandong Province under Grant 2021CXGC010701 and the National Natural Science Foundation of China-Shandong Province under Grant U1706228.

*Corresponding Author: maxin@sdu.edu.cn

Full postal address: 17923 Jingshi Road. Jinan 250061, Shandong, P. R. China

Abstract

During being hoisted into the waves, payloads are subjected to violent hydrodynamic impact, which brings a great challenge for deep-sea cranes' control systems. A two-dimensional numerical model with a motion constraint is established using OpenFOAM software to investigate the water entry of a cylinder into waves with the cavity effect. The accuracy of the numerical model is first verified by the water entry of a cylinder into the calm water. The mesh convergence analysis indicates that the jet profile is highly dependent on the mesh close to the cylinder surface. For the simulation of hoisting the payload into waves, a constraint for the 6 DOF rigid body motion solver is introduced, which can simulate the cylinder lowering in the air with a constant velocity and then falling freely into the wave. With the proposed model in this paper, the water entry of a cylinder into waves is analyzed by dividing the entry process into four stages. Various case studies are carried out to investigate the physical effects of the entry position (crest, trough, upward point, and downward point), and the entry velocity on the hydrodynamic forces, pressure distribution, and free surface profile. Numerical results indicate that the wave particle velocity and wave slope are the essential factors for the asymmetry of pressure on the cylinder. The results also show that the cavity that forms above the cylinder top surface causes a sharp fluctuation of the hydrodynamics force on the cylinder and the cavity volume is positively related to the effective entry velocity. All of the numerical simulation results provide the fundamentals for further research and safe control of offshore lifting or lowering.

Keywords: Water entry; Cylinder entering waves; Cavity effect; Computational fluid dynamics; OpenFOAM

1. Introduction

Hoisting a payload into waves by a deep-sea crane is a very complicated problem, where extremely violent hydrodynamic impact forces can severely damage the payload and the cable, thus threatening the safety of the crew and equipment. Furthermore, the complex and varying hydrodynamic forces also bring great challenges to the design of the crane control system, especially when the wave environment causes more non-linear characteristics. Therefore, exploring the features of the wave entry process of the payload is fundamentally important to the operation and controller design of deep-sea cranes.

The study of water entry has received considerable attention for many years. Based on the law of conservation of momentum, Von Karman (1929) proposed a method to roughly estimate the impact force on the seaplane during landing on calm water, which is considered as a pioneering work on the water entry problem. Further, Wagner (1932) proposed an analytical solution for the water entry by considering the uprise of water along the side of the wedge. Von Karman and Wagner laid the theoretical foundation for the study of water entry. Based on the Wagner theory with matched asymptotic expansions, some researchers investigated the water entry of a wedge with small deadrise angles (Howison et al., 1991) and a wedge with elastic deformations (Korobkin et al., 2006). Dobrovol'skaya (1969) proposed similar solutions for the water entry of wedges with a constant velocity by improving the Wagner theoretical solution. Zhao and Faltinsen (1993) used the boundary element method (BEM) to study the water entry of wedges with different deadrise angles and extended it to a general asymmetric wedge. Semenov and Iafrati (2006) studied the vertical entry of an asymmetric wedge and Xu et al. (2008) solved the problem of the oblique water entry of an asymmetrical wedge. By introducing the auxiliary function to decouple the mutual dependence of the body motion and the fluid flow, Wu et al. (2004) obtained the solution for the water entry of a wedge in free-fall motions. Wang et al. (2015) conducted experiments to investigate the water entry of a freefall wedge with an air cavity. Xu et al. (2010) and Bao et al. (2017) studied the water entry of a wedge in three degrees of freedom, considering the rotational motions of the wedge. However, the potential flow theory has a limitation in treating strongly nonlinear problems (Lin et al., 2021).

For such complex problems, Computational Fluid Dynamics (CFD) methods can capture highly nonlinear free-surface effects for the water entry problem, such as the wave breaking induced by slamming (Chen et al., 2019). Based on the weakly compressible SPH solver (Bouscasse et al., 2013), Sun et al. (2018) applied the adaptive particle refinement (APR) technology in the SPH method to improve the accuracy of free surface solutions. Chen et al. (2020) calculated the water entry impact force on the autonomous underwater helicopter by the CFD analysis software STAR-CCM+. Ma et al. (2018) and Chen et al. (2019) investigated the water entry problem using the open-source CFD package OpenFOAM which uses the VOF method to capture the free surface, and the OpenFOAM has also been used for the water entry problems in the study of Xiang and Guedes Soares (2020) and Xiang et al. (2020).

Most of the above studies mainly focused on the water entry of a wedge, however, the water entry of a cylinder is often considered more challenging and more practical compared with wedges in ocean engineering. Cointe and Armand (1987) investigated the water entry of a cylinder by the Wagner theory. With the CFD analysis software, such as ANSYS Fluent and OpenFOAM, the impact forces and the motion of a cylinder during the water entry were solved (Jiang et al., 2016; Xiang and Guedes Soares, 2020; Xiang et al., 2020). However, some CFD software cannot handle some cylinder entry problems well, since the deadrise angle of the cylinder is very small at the initial stage which can cause singularity, rapidly increasing wetted surface, and large pressure peaks (Larsen, 2013). By comparing the free jet separated from the cylinder surface with three different CFD software packages, Derakhshanian et al. (2018) found that the ABAQUS software is the most capable software for solving the separation point of the jet flow and the results simulated by the other two CFD software are not consistent with the physical experiment conducted by Greenhow and Lin (1983). To calculate the jet distribution in agreement with the experimental observation, Sun et al. (2018) optimized the fluid-body interface by applying the particle shifting technique (PST) modification in the SPH method.

The above literature is limited to the water entry into the calm water without taking into account the incident wave which can bring more nonlinear features for the water entry process. Because of the horizontal velocity of the wave, the body equivalently impacts the water obliquely even the entry velocity is vertical. Sun et al. (2015) investigated the water entry of a two-dimensional symmetric wedge with the constant velocity into a wave using the boundary element method (BEM). They found that the effect of gravity on the pressure coefficient distribution and free surface profile becomes more pronounced as the entry time increases. Wang et al. (2021) simulated the whole process of asymmetric wedge entry into waves and analyzed the pressure distribution and hydrodynamic forces using the OpenFOAM. Cheng et al. (2018) developed a time-domain higher-order boundary element method (HOBEM) to investigate the wedge entry into waves with the wave-current effect, and Cheng et al. (2019) obtained the solution of the wave entry of a wedge in three degrees of freedom. Chen et al. (2022) studied the wave effect on the water entry of a 3D full-scale symmetric wedge by classifying the process into early, vertical-down, and bounce-up stages. Some satisfactory solutions for the water entry of a semi-circular with the cavity effects were also obtained based on the potential flow theory (Cheng et al., 2021; Sun et al., 2019). However, the study of the wave entry of a cylinder using the CFD analysis is very rare, and more understanding of the hydrodynamic characteristics of wave entry is essential for the better design of offshore cranes.

In this paper, the entire water entry process of a cylinder into waves with gravity is numerically simulated using the OpenFOAM. We discuss the comprehensive mechanisms of wave effect on the hydrodynamic force of the cylinder with the pressure distribution and free surface profile. The effect of entry position and entry velocity on the hydrodynamic force of the cylinder is analyzed. The contributions of the paper are as follows: (1) A detailed analysis of the convergence of the sub-mesh is presented to find the appropriate mesh distribution for the accuracy of the jet profile during water entry. (2) According to the acceleration curve, the entire process of wave entry can be classified into four stages, i.e. the impacting stage, jet formation stage, cavity closure stage, and sinking stage. The effects of entry position and entry velocity on the pressure distribution, free surface profile, and hydrodynamic force during these four stages are discussed. (3) The formation and development of the jet and cavity are elaborated, and the mechanisms of cavity effects on the hydrodynamic force are analyzed with pressure and free surface distribution.

The remainder of the paper is organized as follows. Section 2 describes the numerical model and the underlying numerical solution methodology. In Section 3, the test case of water entry of a cylinder into the calm water is first conducted to verify the presented numerical model, and a convergence study is performed. In Section 4, the wave effects on the water entry of the cylinder are analyzed, and the detailed results of the effects of entry position and entry velocity on the cylinder entering waves are provided. Finally, conclusions are drawn in Section 5.

2. Mathematical formulation

2.1 Governing equation

The water entry problem is solved by an *overInterDyMFoam* solver in the OpenFOAM, which combines the incompressible two-phase pressure-based solver *interFoam* and the dynamic overset technology. The governing equations in the two-dimensional incompressible, isothermal, and immiscible fluid domain are the mass conservation and momentum conservation equations, which are given as follows:

$$\nabla \cdot \mathbf{u} = 0 \tag{1}$$

$$\frac{\partial \rho \mathbf{u}}{\partial t} + \nabla \cdot (\rho \mathbf{u}\mathbf{u}) = \nabla \cdot (\mu \nabla \mathbf{u}) - (\mathbf{g} \cdot \mathbf{x}) \nabla \rho - \nabla p_d \tag{2}$$

where $\mathbf{u}$ is the velocity vector, ρ the density of the fluid, t the time, μ the dynamic viscosity of the fluid, $\mathbf{g}$ and $\mathbf{x}$ the gravitational acceleration and the position vector respectively. p_d is the dynamic pressure, which is given by:

$$p_d = p - \rho \mathbf{g} \cdot \mathbf{x} \tag{3}$$

where p is the total pressure.

2.2 Free surface capturing method

The volume of fluid (VOF) method is applied in this model to capture the free surface. In the VOF method, the volume fraction $\alpha \in [0,1]$ represents the water component per unit volume at each cell which is solved by a transport equation:

$$\frac{\partial \alpha}{\partial t} + \nabla \cdot \mathbf{u}\alpha + \nabla \cdot \mathbf{u}_c \alpha (1-\alpha) = 0 \tag{4}$$

where $\nabla \cdot \mathbf{u}_c \alpha (1-\alpha)$ is introduced to limit the numerical diffusion and $\mathbf{u}_c$ is referred to as the compressive velocity field (Chen et al., 2014). The free surface can be identified by tracking the computational cells whose volume fraction α is between 0 and 1. The above equations are integrated over each computational cell to solve α and $\mathbf{u}$, and the dynamic pressure p_d is obtained by solving the pressure corrector linearized equation (Ma et al., 2018).

2.3 Solution algorithm

The solution procedure relies on the PIMPLE algorithm which essentially combines the Pressure-Implicit with Splitting of Operators (PISO) and Semi-Implicit Method for Pressure Linked Equations (SIMPLE). The flow chart of the solution algorithm (Chen et al., 2019) is shown in Fig. 1. Within each PIMPLE loop, the six DOF motion equation is solved first, with the update of the dynamic mesh. Then the free surface is captured by solving the transport equation for the volume fraction field α. The pressure Poisson equation is solved iteratively by the PISO algorithm to deal with the velocity-pressure coupling. Finally, the turbulence modeling equations are solved in the last step. More details of the solution process can be found in Ferro et al. (2022).

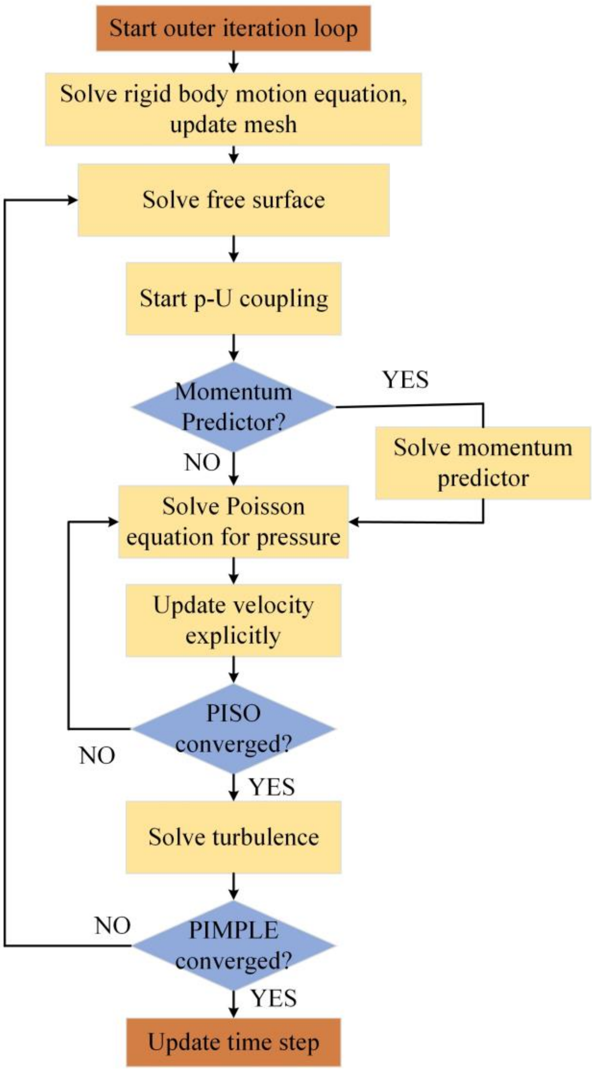

Fig. 1 The flow chart of the solution algorithm.

This work uses built-in numerical schemes in OpenFOAM to numerically approximate the PDE terms in the governing equations and the transport equation for the water volume fraction. **Table 1** shows the discretization schemes in the simulations.

Table 1 The discretization of PDE terms.

	Term	Discretization
Spatial domain Temporal Scheme	ddtSchemes (d/dt)	Finite Volume Method (FVM) Euler, First order implicit, Bounded.
Gradient Schemes	default	Gauss linear, Second order, Unbounded
	$(\nabla \mathbf{u}, \nabla \alpha)$	Gauss linear, Second order, Unbounded
Divergence Schemes	$\nabla \bullet (\rho \phi \mathbf{u})$	Gauss limitedLinearV 1, Second order, Bounded
	$\nabla \bullet (\phi \alpha)$	Gauss vanLeer, Second order, Unbounded
Laplacian Schemes	∇^2	Gauss linear corrected, Second order, Unbounded
Interpolation Schemes	default	Linear, Second order
Surface normal gradient Schemes	default	Corrected, Second order

2.4 Six DOF motion solver

The motion of the free-falling cylinder for the wave entry problem is solved by using the *sixDoFRigidBodyMotion* solver in the OpenFOAM. The cylinder motion is calculated according to the resultant force $\mathbf{F}$ and moment $\mathbf{M}$, which are induced by the pressure and shear stress on the cylinder surface, and the gravity force. The accelerations of the translation $\mathbf{a}$ and rotation $\boldsymbol{\psi}$ for the cylinder motion are obtained from the motion equation which is based on the linear and angular momentum conservations. The motion equations are given by:

$$\mathbf{a} = \mathbf{F} / m \tag{5}$$

$$\boldsymbol{\psi} = \mathbf{I}^{-1} \cdot \mathbf{M} \tag{6}$$

where m is the mass of the cylinder and $\mathbf{I}$ denotes the moment of inertia.

The body position and rotation solving process are essentially the same, so the position is presented as an instance to illustrate the solution process of the *sixDoFRigidBodyMotion* solver. The acceleration relaxation coefficient χ is used to improve the stability of the motion solver:

$$\mathbf{a}_n = \chi \mathbf{a} + (1-\chi)\mathbf{a}_o \tag{7}$$

where $\mathbf{a}$ are obtained from Eq. (5). The subscripts of *n* and *o* indicate the acceleration at the new and old time steps, respectively. According to the linear acceleration $\mathbf{a}_n$, the current linear velocity and position can be updated using the Newmark integration scheme strategy, which is expressed as:

$$\boldsymbol{v}_n^{k+1} = \boldsymbol{v}_o + \Delta t(\gamma \mathbf{a}_n^k + (1-\gamma)\mathbf{a}_o) \tag{8}$$

$$\boldsymbol{l}_n^{k+1} = \boldsymbol{l}_o + (\mathbf{u}_o \Delta t + \gamma (\Delta t)^2 (\beta \mathbf{a}_n^k + (0.5-\beta \mathbf{a}_o))) \tag{9}$$

where $\boldsymbol{v}$ is the velocity of the cylinder, and $\boldsymbol{l}$ is the position of the center of rotation. The coefficients β and γ are typically set to 0.5 and 0.2, which yields the so-called constant average acceleration method. The superscript k represents the sub-iteration step for the implicit sub-iterations in time (Chen et al., 2019).

At the wave generation stage, the motion solver for updating the linear and rotational displacements is restrained. After several periods of waves that fully develop, the constraint allows the cylinder to fall in the air with a constant velocity by limiting the update of the motion velocity. When the cylinder touches the wave surface, the constraint is removed so that the cylinder enters the wave with a free-falling motion.

2.5 Computational domain setup

To describe the wave entry problem, two Cartesian coordinate systems are defined in the computation domain: a global coordinate system $OXYZ$ fixed on the numerical tank bottom and a body-fixed coordinate system $oxyz$ on the body. As shown in Fig. 2, the X axis is along the wave propagation direction, with the Z axis pointing upwards. The body-fixed coordinate system $oxyz$ is placed at the mass center of the cylinder and moves with the cylinder. Fig. 2 shows that the rectangular computational domain for the wave entry is divided into two parts which are the wave generation zone and the impact zone. The 5th order Stokes wave is generated in the computational domain by a wavemaker placed on the left side. The active absorption method (Schäffer Hemming and Klopman, 2000) is applied to avoid wave reflection from the outlet boundary.

As shown in Fig. 2, the numerical tank defines 6 boundaries named **Inlet**, **Outlet**, **Front and Back**, **Bottom**, **Atmosphere**, and **Cylinder**, respectively. Each boundary requires a set of boundary conditions to define boundary variables including the velocity, pressure, and phase fraction. The boundary conditions used in this work are given in Table 2, which are standard OpenFOAM boundary conditions. Due to two-dimensional simulation, the **Front and Back** boundary of the numerical tank is defined as *empty*. The boundary conditions, *waveVelocity* and *waveAlpha*, are employed for the velocity and phase fraction in the **Inlet** boundary to specify the wave values from wave models. The *pressureInletOutletVelocity* is used for the **Atmosphere** boundary that is free to the atmosphere. This boundary is a blend of *pressureInletVelocity* and *inletOutlet* boundary conditions, which apply a *zero-gradient* condition for the outflow and switch to *fixedValue* to the reverse flow. The velocity boundary of the **Cylinder** is *movingWallVelocity* which corrects the flux for moving boundaries to ensure that the normal velocity flux across the boundary surface is zero. The *fixedFluxPressure* condition sets the pressure to ensure that the flux matches the velocity boundary condition, and the *totalPressure* condition is used to set the pressure to zero on the atmosphere boundary (Aliyar et al., 2022).

Table 2 Boundary conditions in the numerical tank.

Boundary	Velocity	Pressure	Phase fraction
Inlet	*waveVelocity*	*fixedFluxPressure*	*waveAlpha*
Outlet	*waveVelocity*	*fixedFluxPressure*	*zeroGradient*
Atmosphere	*pressureInletOutletVelocity*	*totalPressure*	*inletOutlet*
Bottom	*fixedValue*	*fixedFluxPressure*	*zeroGradient*
Cylinder	*movingWallVelocity*	*fixedFluxPressure*	*zeroGradient*
Front and Back	*empty*	*empty*	*empty*

The overset mesh model consists of the background mesh and the body-fitted component mesh to handle the large-amplitude motions of the moving objects. The background mesh is mainly used to calculate the fluid value of the water entry environment including the wave elevation, water particle velocity, pressure, etc. As shown in the overview of the computational mesh in Fig. 2(b), the background mesh is refined at the free surface area in the vertical direction for generating the wave accurately. Furthermore, small mesh elements are also used in the impact region ensuring a good resolution for the violent flow. To save computational resources, the coarse mesh is used in the areas with smooth value variations, such as the bottom and left areas of the computational domain.

The cylinder is modelled in the sub-mesh, which is generated on top of the background mesh. Fluid values are exchanged between different meshes using interpolation in the fringe region of the sub-mesh (Chen et al., 2019). The sub-mesh is an essential part to capture the slamming pressures and the jet surface accurately.

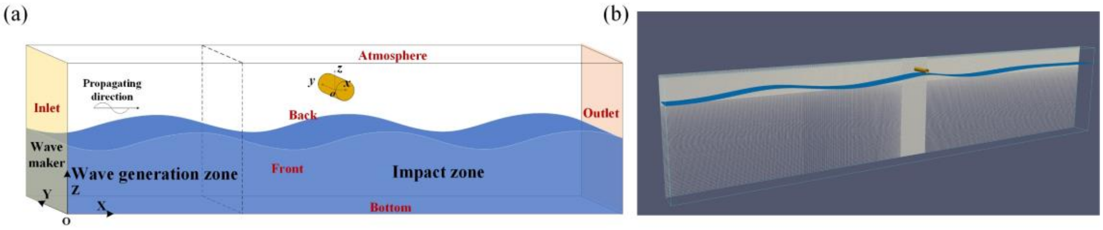

Fig. 2 Numerical setup of wave entry of a cylinder: (a) sketch of the cylinder entering waves; (b) snapshot of the background mesh in the OpenFOAM.

3. Model validation and convergence study

The experimental investigation of a cylinder free-falling into the calm water conducted by Greenhow and Lin (1983) is reproduced numerically to verify the presented model. In the experiment, two cylinders with a radius of 0.055 m are dropped into the calm water from a height of 0.5 m above the free surface. The masses of the two cylinders are 9.4985 kg and 4.737 kg corresponding to the neutral buoyancy and half of the neutral buoyancy respectively. In the numerical simulation, the cylinder is held still at the free surface and then it freely falls into the calm water with an initial velocity of v = 2.938 m/s.

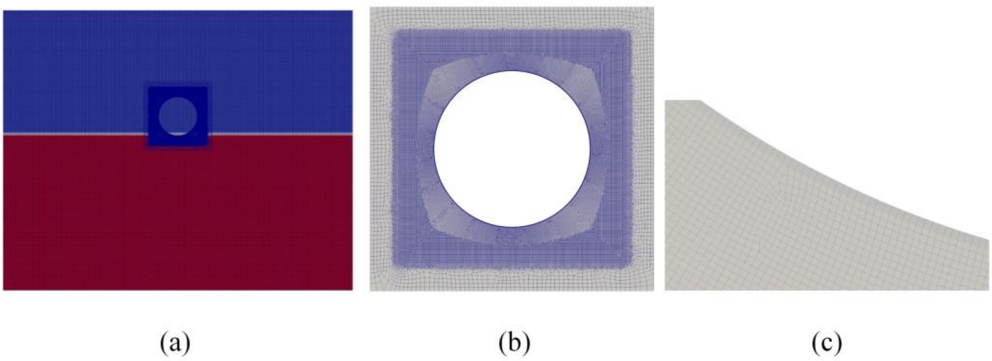

Fig. 3 Overset mesh for the cylinder entering the calm water: (a) overview of the computational domain; (b) sub-mesh modelling the cylinder; (c) close-up view of the sub-mesh near the cylinder

surface.

The numerical results of water entry problems are affected by the mesh quality near the body surface, which means that the sub-mesh resolution plays a dominant role in the water entry results. Therefore, in the convergence analysis, the influence of the sub-mesh on the pressure and free surface is mainly considered. The rectangular computational domain in Fig. 3(a) for the water entry problem is set to 1 × 1 × 0.8 m with a water depth of 0.5 m. The background mesh is discretized with the uniform regular hexahedral cells where the mesh resolution is $\Delta x = \Delta z = 0.006$ m. As shown by the generated sub-mesh around the cylinder in Fig. 3(b), the mesh resolution in the fringe of the sub-mesh is the same as the background mesh, which ensures the accuracy of the interpolation. For solving the slamming pressure and the free surface profile accurately, the inner area is refined using an adequate number of elements and well-organized grids.

At the early stage of the water entry, the small deadrise angle and the rapidly increasing wetted surface cause some challenging problems including the inaccurate impact pressure, the oscillating slamming force, and especially the incorrect jet profile. Thus, referring to the work in Larsen (2013), the mesh layer close to the cylinder surface with 1mm thickness is modelled with the prism layer mesh which is shown in the close view of the sub-mesh in Fig. 3(c).

Most cases in this paper are computed using a workstation with the Intel Xeon (R) E5 2699v4 CPU, 128G RAM, and the cases for the convergence study are computed with 8 cores. **Table 3** lists different parameters of the sub-mesh schemes including the resolution of the refinement area, the number of prism layer, and the total cell number. The maximum Courant number is set to 0.5, and the adaptive time step is adopted.

Table 3 Sub-mesh parameters and computational cost for the cylinder freely falling into the calm water.

Mesh scheme	Refined cell size $\Delta x = \Delta z$	Prism layer mesh number	Cell number:	Run time (h): (half buoyancy/neutral buoyancy)
1	0.0008	5	293	4.1/6.8
2	0.0008	8	307	6.7/7.4
3	0.0005	5	683	13.2/11.9
4	0.0005	8	703	12/12.2
5	0.0004	5	104	26.8/25.3
6	0.0004	8	107	32.5/33.6

The time history of the vertical force on the cylinder using different mesh schemes is shown in Fig. 4. It can be observed that the vertical force agrees well with the numerical result in Larsen (2013), which confirms the capability of the present model. Fig. 4 indicates that even the coarsest Mesh 1 can provide an accurate vertical force solution. The force fluctuations at the initial phase are caused by the pressure peak in the jet root region which is smaller than the mesh size (Larsen, 2013). However, some mesh schemes do not model the splash correctly as shown in Fig. 5. It can be seen that the jets obtained with Mesh 1 do not separate from the cylinder surface and the free surface seems unreal. Therefore, the convergence study for the jet profile is also carried out to find a high-quality mesh to ensure accurate solutions. For the sake of brevity, only the free surface of the neutral buoyant cylinder is analyzed in detail.

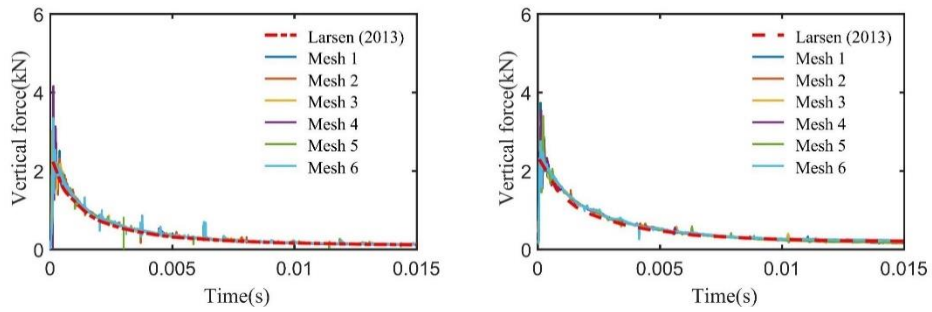

Fig. 4 Comparison of the force-time curve using different mesh schemes: (a) half buoyancy; (b) neutral buoyancy.

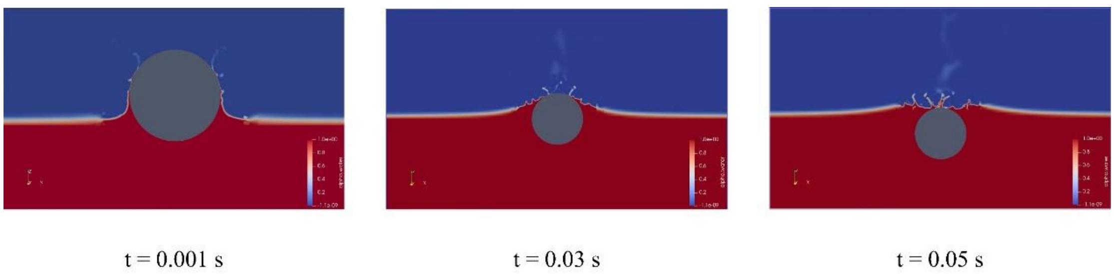

Fig. 5 Free surface of the cylinder free-falling into the calm water using Mesh 1.

Comparisons of the free surface profile at t = 0.015 s using six different mesh schemes with the experiment data are shown in Fig. 6. For Mesh 1 and Mesh 5, the jet uprises along the cylinder surface and appears the unphysical flow pattern which may be due to the fact that the prism layer mesh is too coarse to separate the jet flow. Although the jet flow is separated from the cylinder surface in Mesh 2 and Mesh 3, the separation point does not match the experiment result. The free surface results using Mesh 4 and Mesh 6 are in the best agreement with the experimental results, including the correct separation position and the jet profile. It can be concluded that the finer prism layers mesh can obtain the correct separation position, and the outer quadrilateral grid determines the correct shape of the free surface. Although the refined prism layers mesh can help with the jet separation, if the prism layers mesh resolution is too small to mismatch the outer quadrilateral mesh size, it may also cause incorrect free surface results.

It is worth noting that the incorrect jet does not significantly influence the results of the initial slamming force on the cylinder, since the tip of the jet does not contribute much to the solution of the pressure in the initial stage. As the penetration depth increases, the unseparated fluid above the cylinder exerts pressure on the cylinder, resulting in the incorrect solution of the vertical force on the cylinder.

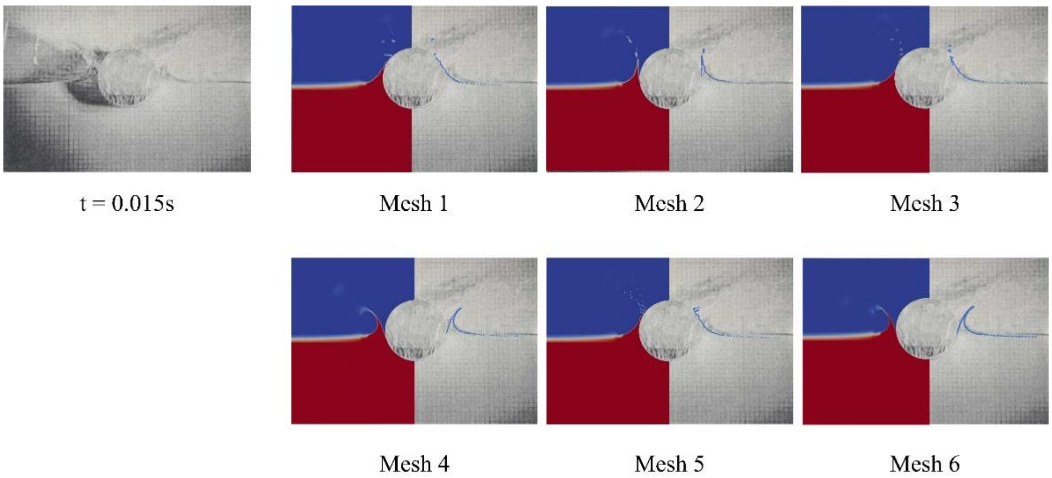

Fig. 6 Comparison of the free surface between the experimental measurement (Greenhow and Lin, 1983) and the numerical simulations with different mesh schemes.

4. Water entry of a cylinder into waves

4.1 Effect of wave on water entry of a cylinder

This section mainly investigates the influence of the Stokes wave on the water entry of a free-falling cylinder with an initial velocity. A sketch of the simulation setup and the meshing scheme of the cylinder entering the wave is given in Fig. 2 where the length and width of the computational domain are set to 24 m and 5 m. The 5th order Stokes wave with the wave height H = 0.3 m and wave period T = 2.2 s is generated from the left side of the numerical wave tank with the water depth h = 4 m. A cylinder of the radius 0.1 m impacts the wave crest with an initial velocity v = 1 m/s in the numerical simulation. The mass of the cylinder is set as 37.68 kg, corresponding that the density of the cylinder is 1.2 times the fluid density.

Prior to the simulations of wave entry, simulations without cylinder motion are performed to verify the accuracy of wave making. Fig. 7 shows the time histories of the wave elevation below the cylinder compared to the solution by Skjelbreia and Hendrickson (1961). A fairly good agreement between the standard result and the simulation is obtained except for the initial three wave cycles since the wave is generated in a numerical wave tank by the wave velocities with a smooth time ramp.

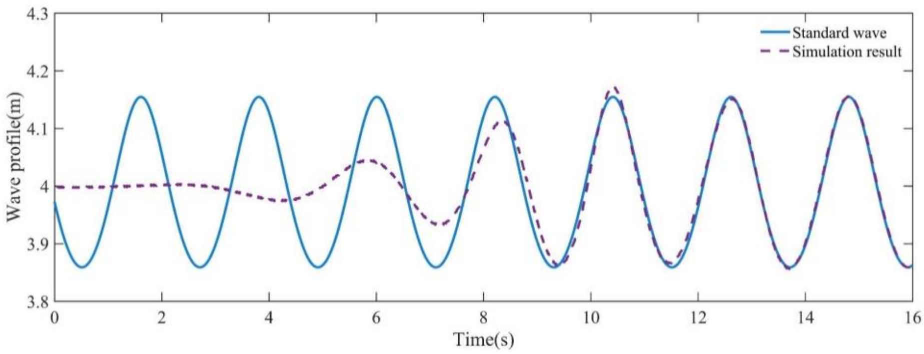

Fig. 7 Comparison of wave elevation between the undisturbed simulated wave and standard wave by Skjelbreia and Hendrickson (1961).

Since the force on the cylinder is proportional to the acceleration, the time history of the cylinder acceleration is plotted during the entry time t = 0-0.6 s in Fig. 8. According to the acceleration of the cylinder, the wave entry process can be divided into 4 distinctive stages: impacting stage, jet formation stage, cavity closure stage, and sinking stage, which are also distinguished by different colours in Fig. 8. The vertical force decreases in the impacting stage (t = 0-0.03 s) and then increases in the jet formation stage (t = 0.03-0.3 s), while the horizontal force changes in the opposite manner. During the cavity closure stage (t = 0.3-0.4 s), the vertical and horizontal forces decrease sharply as the compressed cavity exerts violent pressure on the top surface of the cylinder. Finally, in the sinking stage (t = 0.4-0.6 s), the cylinder is fully submerged in the wave, and its vertical force gradually increases with the penetration depth.

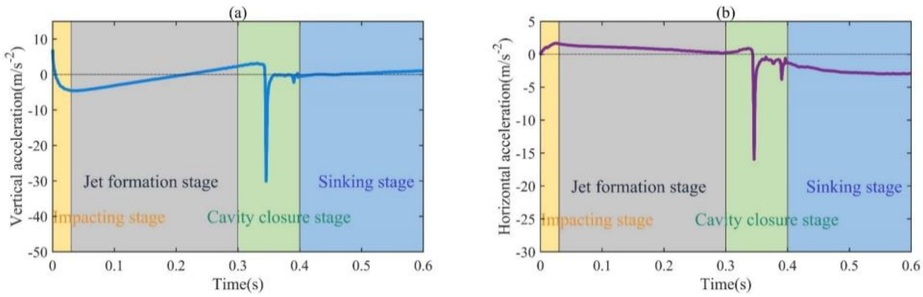

Fig. 8 Time history of acceleration of the cylinder falling into the wave crest: (a) vertical acceleration; (b) horizontal acceleration.

Fig. 9 shows the cylinder position in the global coordinate system and the red curve represents the entry trajectory of the cylinder centre. It can be seen that the cylinder moves to the right at the initial entry stage, and shifts leftward after the cavity closure stage, which corresponds to the change in the horizontal force.

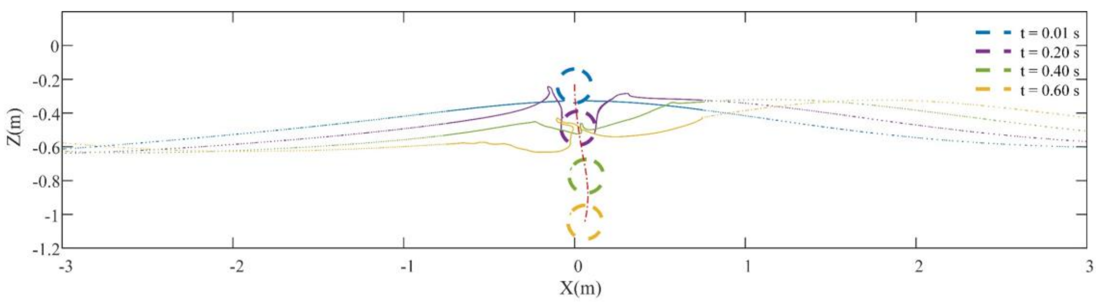

Fig. 9 Position of the cylinder in the global coordinate system at different time instants.

4.1.1 Impacting stage

When the cylinder touches the wave surface with the initial velocity, the cylinder is subjected to a large hydrodynamic impact. Then, the vertical force on the cylinder rapidly decreases as the penetration depth increase. This is different from the phenomenon of a continuous increase in the vertical force during a wedge entering waves (Wang et al., 2021). The reason for this phenomenon is the increase in the effective deadrise angle of the cylinder, which can be seen in detail by the free surface distribution and pressure distribution. To clearly show the pressure distribution, an angle $\theta \in [0, 2\pi)$ is defined in Fig. 10 to show the pressure distribution along the cylinder's circumference. As shown in Fig. 11, the effective deadrise angle between the cylinder and the wave surface is zero at the impact instant, resulting in high pressure on the cylindrical wetted surface. Since the effective deadrise angle between the cylinder and the wave surface increases, the pressure and the vertical force on the cylinder decrease rapidly.

Fig. 11(a) illustrates the changing characteristics of the pressure distribution in the impacting stage. During t = 0.01-0.02 s, the pressure on the cylinder is maximum at the jet-root region which is similar to the pressure distribution for the wave entry of a wedge (Sun et al., 2015). As the cylinder moves downward, the pressure peaks on the jet roots gradually shift to the centre of the cylinder's bottom surface. It is also interesting that the pressure on the jet top is negative, which means that the pressure is smaller than the atmospheric pressure. This feature may be due to the air being trapped in that region. In addition, the pressure on the left side of the cylinder is larger than that on the right side, resulting in a horizontal force pointing to the right. This is because the wave particles at the crest have a horizontal velocity in the rightward direction, which is equivalent to a body entering the calm water with a horizontal velocity in the leftward direction. Therefore, the cylinder entering the wave at the crest can be treated as the oblique entry during t = 0.01-0.02 s.

In the impacting stage, Fig. 11(b) shows that the jet uprises along the cylinder surface, and most of the jet flow still clings to the cylinder surface. Because of the horizontal wave particle velocity, the jet on the left side of the cylinder is slightly higher than that on the right side.

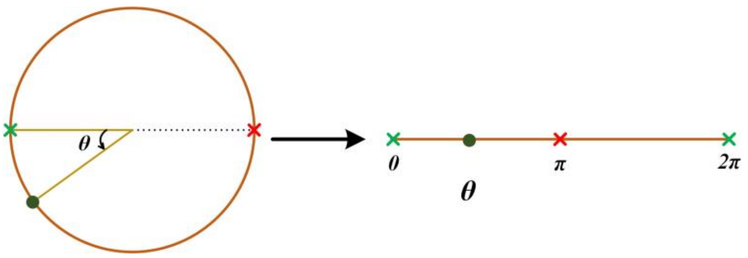

Fig. 10 Definition of the angle $\theta \in [0, 2\pi)$ for plotting pressure distribution.

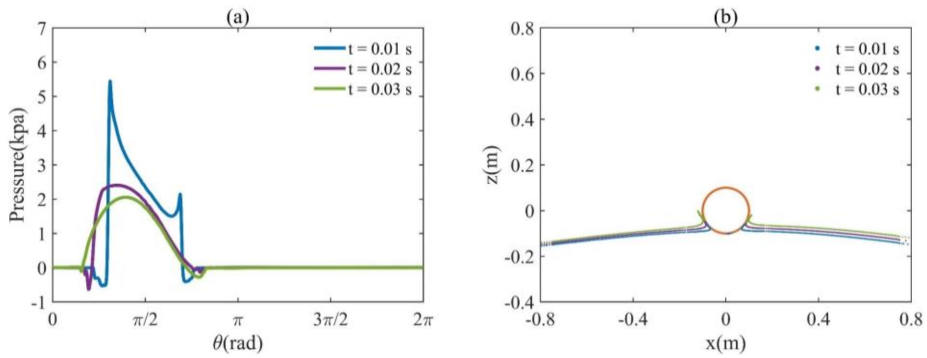

Fig. 11 Pressure and free surface results of a cylinder entering the wave crest in the impacting stage: (a) pressure distribution; (b) free surface profile.

4.1.2 Jet formation stage

As the cylinder moves downward, the vertical force on the cylinder gradually increases due to the increase of the entry velocity and the impact/wetted area. After t = 0.213 s, the vertical force is greater than the gravity causing the vertical entry velocity of the cylinder to decrease. Because the horizontal velocity of the wave particle decreases as the depth increases. The horizontal force on the cylinder gradually decreases, which causes the horizontal velocity of the cylinder increases more and more slowly.

Fig. 12(a) shows the pressure distribution in the jet formation stage. As the horizontal velocity of the wave particle decreases as the depth increases, the pressure on the cylinder bottom surface becomes symmetric gradually, and the maximum pressure shifts toward the centre of the cylinder bottom. The negative pressure near the jet root regions also gradually disappears. In Fig. 12(b), the jet separates from the cylinder surface in the form of a splash. Because of the horizontal velocity of the wave particle, the jet on the left side is longer than that on the right side. The vertical velocity of the jet rapidly decreases and the jet eventually falls into the wave due to the effect of gravity. The jets pile up with the incident wave, and the left and right jet roots form the depart flow moving towards each other at t = 0.3 s. Then the depart flow moves inwards because of the gravity and the push effect of the incident wave, forming a cavity on the top side of the cylinder.

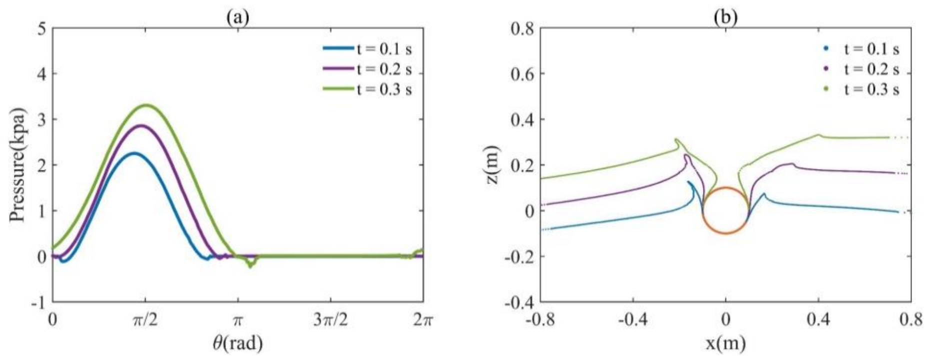

Fig. 12 Pressure and free surface results of a cylinder entering the wave crest in the jet formation stage: (a) pressure distribution; (b) free surface profile.

4.1.3 Cavity closure stage

In Fig. 13, as the cylinder moves downwards, the inner surface of the jet flow moves inwards due to the gravity and push effect of the wave. The left side and right side flows eventually impact each other forming a cavity behind the cylinder. Because of the wave effect, the close position of the cavity is not on the centerline of the cylinder. The left side inner flow touches the cylinder's top surface earlier and exerts a downward and rightward hydrodynamic force on the cylinder before the cavity closure, which is reflected by the larger pressure on the left side of the top surface at t = 0.34 s. Consequently, the horizontal force slightly increases before the cavity closes during t = 0.3-0.34 s shown in Fig. 8. At t = 0.34 s, sharp fluctuations in the vertical and horizontal forces are observed in Fig. 8. This is because the air pocket is compressed by the collision of the left and right depart flows, which results in a sudden increased pressure on the cylinder top surface. The cavity is mainly gathered on the right side of the cylinder's top surface, thus the horizontal force sharply decreases, which means the horizontal force suddenly points to the left.

The pressure and free surface distribution during the cavity close stage are illustrated in Fig. 14. At t = 0.35 s, the cavity is closed and compressed by the inward free surface. The pressure on the cylinder top surface increases rapidly, which is even higher than the pressure on the cylinder bottom surface. However, the large pressure on the bottom surface rapidly disappears because the air pocket leaves the cylinder's top surface. Fig. 14(b) shows that the closing point of the air cavity is on the right side of the cylinder. After the cavity is closed, an upward jet is subsequently formed by the collision of the free surface.

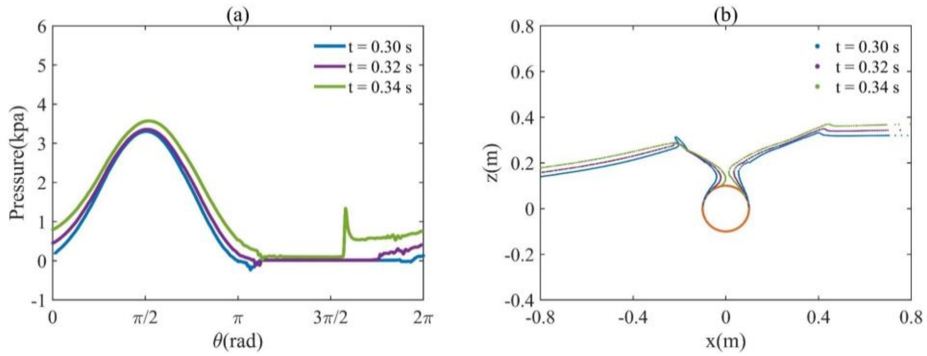

Fig. 13 Pressure distribution and free surface profile of a cylinder entering the Stokes wave before the cavity close: (a) pressure distribution; (b) free surface profile.

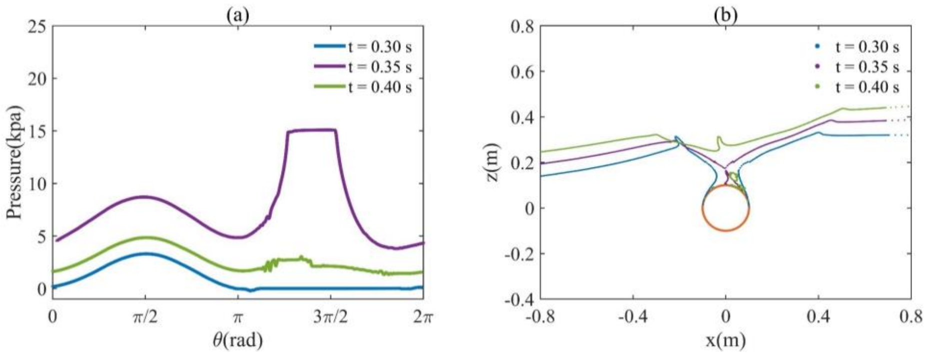

Fig. 14 Pressure distribution and free surface profile of a cylinder entering the Stokes wave in the cavity close stage: (a) pressure distribution; (b) free surface profile.

4.1.4 Sinking stage

At the sinking stage, the vertical force on the cylinder gradually increases with the penetration depth. Fig. 15(a) shows that the pressure on the right top of the cylinder surface is larger than that on the right side. Consequently, the imbalanced pressure distribution leads to an increase in the horizontal force to the left. Fig. 15(b) shows that the bubbles float upward to the free surface from the cylinder surface. The uprise vertical jet bends to the right due to the gravity and the push effect of the incident wave.

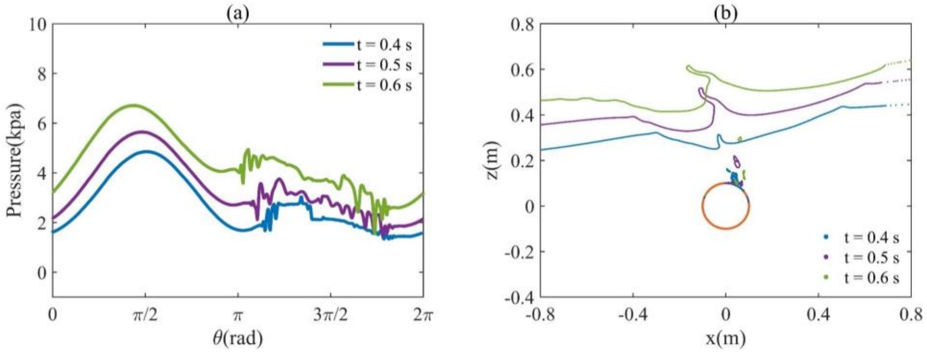

Fig. 15 Pressure distribution and free surface profile of a cylinder entering the Stokes wave in the sinking stage: (a) pressure distribution; (b) free surface profile.

4.2 Effect of the entry position on the wave entry of a cylinder

To study the influence of the entry position, the water entry of the cylinder entering the wave at different wave positions shown in Fig. 16, i.e., the crest, downward point, trough, and upward point, is simulated. Other parameters are the same as in Section 4.1. Fig. 17 shows the comparison of the vertical and horizontal accelerations of the cylinder entering the wave at different entry positions. Moreover, the pressure distribution and free surface profile for different entry positions are plotted in Fig. 18-Fig. 22.

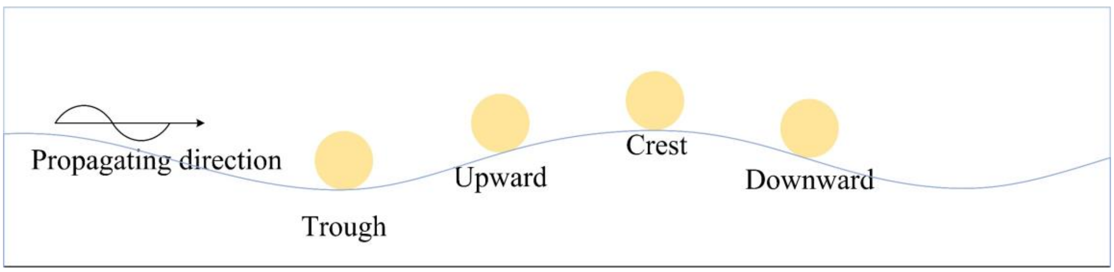

Fig. 16 Water entry position in the Stokes waves.

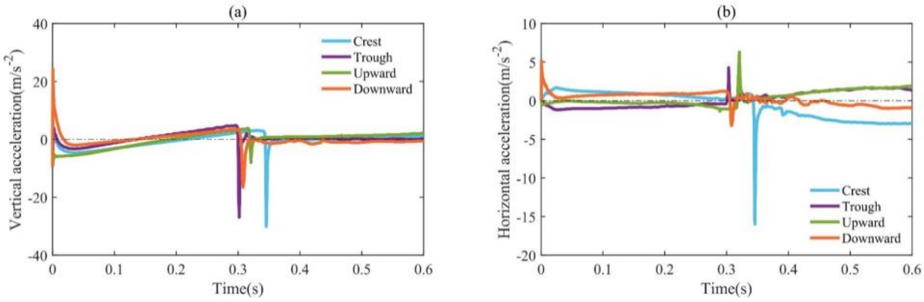

Fig. 17 Acceleration of the cylinder entering the wave at different positions: (a) vertical acceleration; (b) horizontal acceleration.

4.2.1 Effect of the entry position in the impacting stage

In the impacting stage, the vertical impact force is largest in the downward point entry and smallest in the upward point entry as shown in Fig. 17(a). The reason for this phenomenon is mainly contributed by the vertical velocity of the wave particle. The wave particle in the downward point has a vertical-up velocity, which increases the effective velocity between the cylinder and the wave. Correspondingly, the effective velocity decreases at the upward point. The wave particle velocities at the upward point and downward point are -0.4 m/s and +0.4 m/s, which make the effective impacting velocity to be 0.6 m/s and 1.4 m/s, respectively. In the previous study (Wang et al., 2021), it is confirmed that a larger effective impacting velocity causes a larger hydrodynamic force. Fig. 17(b) shows that the horizontal forces in the crest and trough entries are in the opposite direction, which is due to the opposite horizontal velocity of the wave particle at the crest and trough positions. For the wave entry in downward and upward points, the wave slope is the essential factor causing the difference in the horizontal force of the cylinder.

Fig. 18 shows the pressure distribution on the cylinder for different entry positions. Due to the vertical velocity of the wave particle, the downward point entry has the largest pressure, and the pressure is the smallest in the upward point entry. The wedge entry in downward and upward positions can be identified as the asymmetric oblique entry for a symmetric wedge (Chen et al., 2022). However, the cylinder is tangent to the wave surface at the initial stage, with the same angle of relative deadrise angle on both sides, and the entry velocity is not perpendicular to the wave surface. Therefore, cylinder entry in downward and upward points can be regarded as a symmetric oblique entry. Therefore, the pressure distributions in Fig. 18 show that the pressure on the left side of the cylinder is larger than that on the right side of the upward point entry and opposite in the case of the downward point entry. Moreover, the magnitude and area of the negative pressure are also positively related to the effective entry velocity. Due to the difference in the horizontal wave velocity, the pressure distributions in the crest and trough entries are opposite to each other.

As shown in Fig. 18, the jet in the downward point entry has the larger upward velocity and length due to the larger effective entry velocity. In contrast, the jet at the upward point has a smaller vertical velocity causing the jet to bend downward earlier than that in other cases.

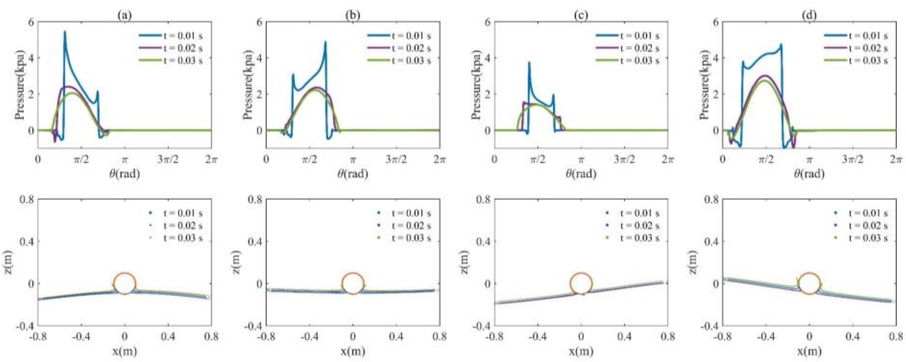

Fig. 18 Pressure distribution and free surface for different entry positions in the impacting stage: (a) crest entry; (b) trough entry; (c) upward point entry; (d) downward point entry.

4.2.2 Effect of the entry position in the jet formation stage

As can be seen from the vertical acceleration curves in Fig. 17(a), the vertical force increases in the jet formation stage. For the crest and trough entries in Fig. 19, the pressure on the bottom surface of the cylinder tends to be symmetrical because the effect of the horizontal velocity of the waves disappears gradually. Therefore, the magnitude of the horizontal force decreases with the penetrating depth for the crest and trough entries. Fig. 19(d) shows that the pressure on the cylinder top surface is positive at t = 0.3 s. This is because the fluid flow above the cylinder moving inward compresses the air in the cavity which increases the pressure in the cavity. In addition, the downward point entry has a longer jet and a larger cavity volume compared to the other cases. The cavity in the upward point entry is incomplete due to the smaller effective entry velocity. For the trough entry, the jet on the right side is higher and steeper than that on the left side, which is opposite to the free surface distribution at the wave crest.

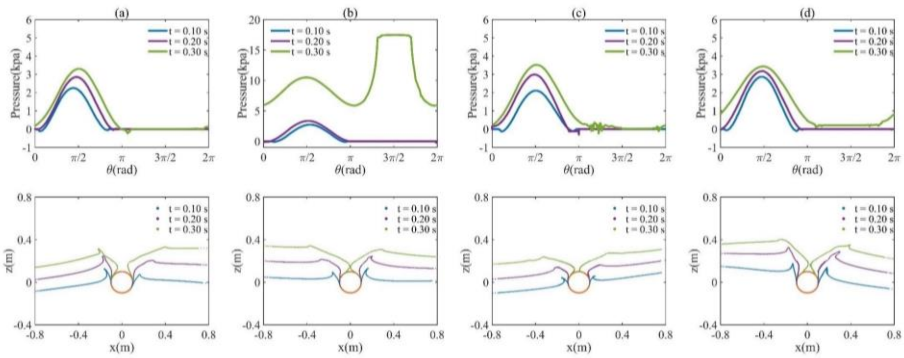

Fig. 19 Pressure distribution and free surface for different entry positions in the jet formation stage: (a) crest entry; (b) trough entry; (c) upward point entry; (d) downward point entry.

4.2.3 Effects of entry position in the cavity closure stage

According to the force curves in Fig. 17 and the free surface profiles in Fig. 20, it can be seen that the cavity closes earliest at the trough entry and last at the crest entry. The close point of the air cavity is on the right side of the cylinder in the crest and downward point entries, which means that the air pocket is concentrated on the right top surface of the cylinder and exerts a horizontal force on the cylinder to the left. Because of the smallest effective entry velocity, the cavity volume in the upward point entry is the smallest, leading to the smaller pressure on the cylinder top surface in Fig. 20. As shown in Fig. 17, the vertical force magnitude in the crest and trough entries is larger, followed by the upwind point entry, and finally the downward point entry. This feature can be explained by the effective entry velocity which is further discussed in Section 4.3.

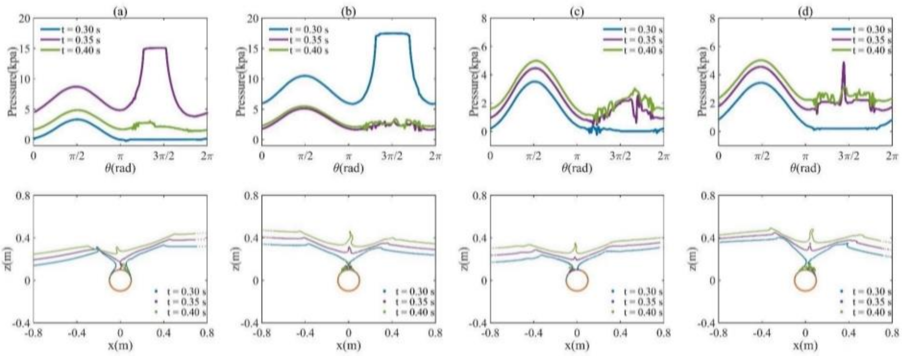

Fig. 20 Pressure distribution and free surface for different entry positions in the cavity closure stage: (a) crest entry; (b) trough entry; (c) upward point entry; (d) downward point entry.

The cavity variation is more complicated in the downward point entry because the cavity volume at the downward point is more complete and larger than in other cases. To better illustrate the process of cavity change after the cavity closure, Fig. 21 shows the pressure distribution and free surface profile during t = 0.332-0.38 s. At the entry time t = 0.332 s, the flow above the cylinder impacts each other and then divides into two parts: one part, namely the inward jet, impacts the cylinder surface downwards and the other part rises upwards forming a new vertical jet. The inward jet divides the cavity into two pockets and the left part has greater pressure than the right part before the inward jet touches the cylinder's top surface. The inward jet hits the cylinder at t = 0.34 s, resulting in a pressure peak on the right upper surface of the cylinder as shown in Fig. 21(b). Then the inward jet generates two horizontal jets along the cylinder surface separating the air pocket from the cylinder surface. As the cylinder continues moving downward, the air pockets gradually leave the top surface of the cylinder and move upward toward the free surface. The air pocket on the right side rises faster than the right side for the downward point entry.

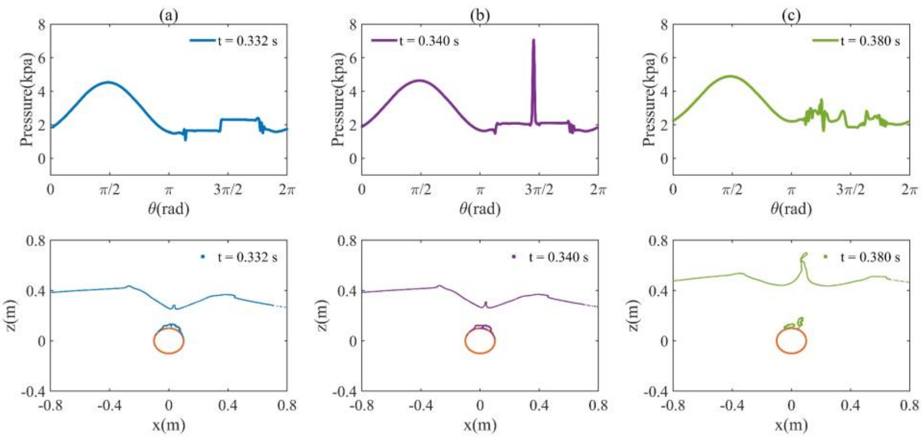

Fig. 21 Pressure distribution and free surface in the downward point entry after the cavity close: (a) t = 0.332 s; (b) t = 0.340 s; (c) t = 0.380 s.

4.2.4 Effects of entry position in the sinking stage

As shown in Fig. 22, the pressure on the top cylinder surface is greater on the side with the bubbles. The reason for this phenomenon can be explained by the vertical velocity contour shown in Fig. 23, where the arrow indicates the fluid velocity, and the arrow color indicates the pressure value. It can be seen that the water particles above the cylinder flow to the air bubbles, resulting in greater pressure on the side of the cylinder surface where the bubbles exist. As shown in Fig. 22, the upward jet is positively correlated with the effective entry velocity.

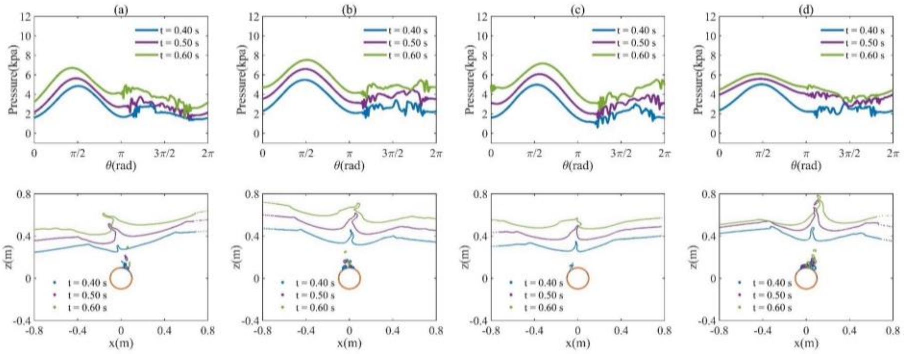

Fig. 22 Pressure distribution and free surface for different entry positions in the sinking stage: (a) crest entry; (b) trough entry; (c) upward point entry; (d) downward point entry.

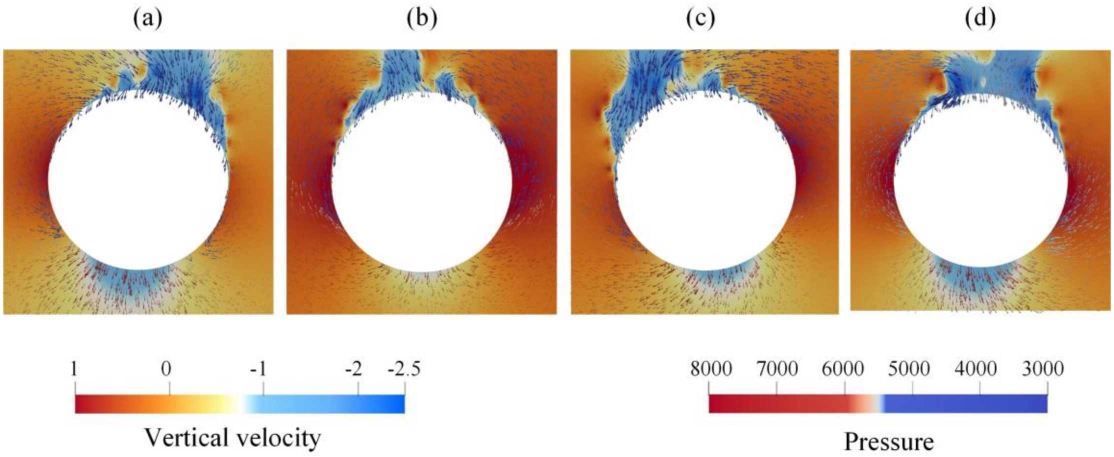

Fig. 23 Vector diagram of flow velocity for different entry positions at t = 0.6 s: (a) crest entry; (b) trough entry; (c) upward point entry; (d) downward point entry.

4.3 The influence of cylinder entry velocity

Three different entry velocities v = 0.5, 1.0, and 1.5 m/s are considered to investigate their influence on the wave entry of a cylinder, including the hydrodynamic force, pressure distribution, and free surface profile. According to the wave particle velocity, the results of the entry velocity effect are divided into two groups for discussion, which are the case of the crest-trough positions and the case of the upward-downward position respectively.

4.3.1 Effects of entry velocity at crest and trough positions

As shown in Fig. 24 and Fig. 25, the entry velocity has a significant influence on the vertical and horizontal accelerations in the impacting stage and the cavity closure stage. In the impacting stage, the impact force on the cylinder becomes greater with the increase of the entry velocity. The larger impact force drops faster at the end of the impacting stage. The larger entry velocity makes the pressure on the cylinder more asymmetric, resulting in a greater magnitude of horizontal force at the impact stage.

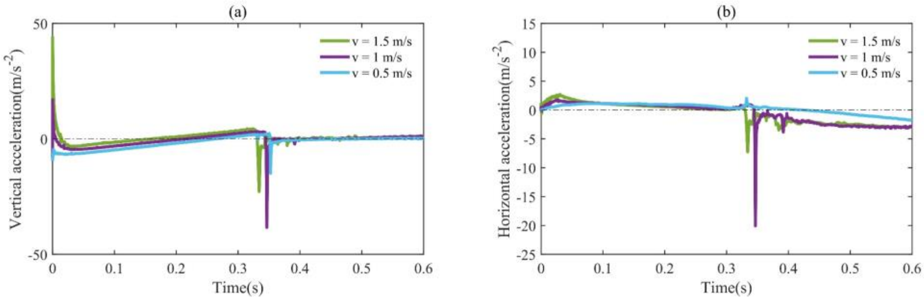

Fig. 24 Comparison of accelerations of the cylinder with different initial velocities in the wave crest entry: (a) vertical acceleration; (b) horizontal acceleration.

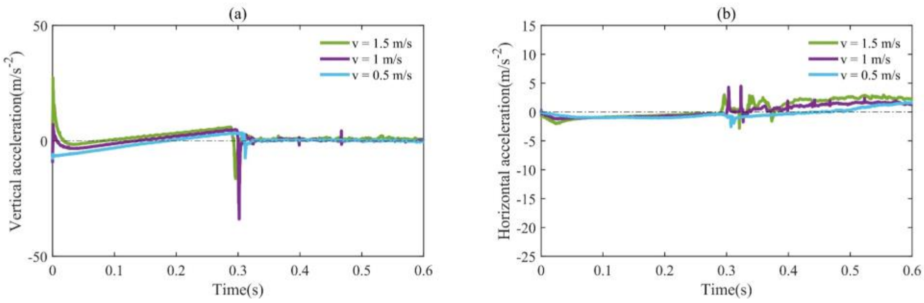

Fig. 25 Comparison of accelerations of the cylinder with different initial velocities in the wave

trough entry: (a) vertical acceleration; (b) horizontal acceleration.

In the cavity closure stage, the compressed cavity exerts a large pressure on the cylinder top surface, which contributes to sharp fluctuations in the vertical and horizontal forces. As observed in Fig. 24 and Fig. 25, it can be concluded that the large entry velocity causes the cavity to close earlier. However, different from the impacting stage, the force magnitude is largest at v = 1.0 m/s, which indicated that the force magnitude is not positively related to the entry velocity at the time of the cavity closure. This phenomenon may be due to the cavity volume at the cavity closure moment as shown in Fig. 26 and Fig. 27. When the entry velocity is v = 0.5 m/s, the cavity is small and incomplete, and then the air pocket is quickly expelled upwards so that the air pocket does not exert a large pressure on the upper surface of the cylinder. In the cases of v = 1.0 and 1.5 m/s, the air pocket has been well developed and the cavity volume increases with increasing the entry velocity. However, for the well-developed cavity, the large cavity volume has a smaller compressed rate, resulting in a negative correlation between the pressure at the top of the cylinder and entry velocity.

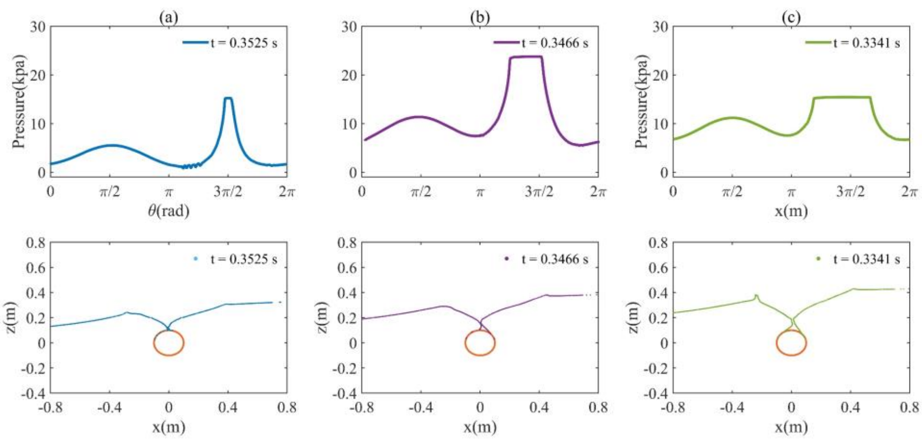

Fig. 26 Pressure distribution and free surface profile in the wave crest entry at the moment of cavity closure: (a) v = 0.5 m/s; (b) v = 1.0 m/s; (c) v = 1.5 m/s.

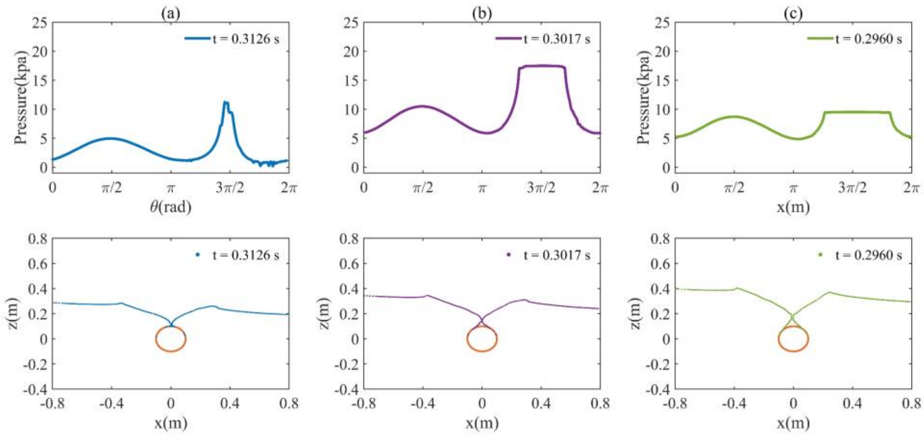

Fig. 27 Pressure distribution and free surface profile in the wave trough entry at the moment of cavity closure: (a) v = 0.5 m/s; (b) v = 1.0 m/s; (c) v = 1.5 m/s.

4.3.2 Effects of entry velocity at upward and downward positions

Fig. 28 and Fig. 29 show the accelerations in the upward point entry and downward point entry respectively. The vertical-down velocity of the wave particle leads to a smaller effective entry velocity in the case of upward point entry. Therefore, the cavities in the upward point entry with v = 0.5 and 1.0 m/s are not complete which leads to the smaller pressure on the top surface of the cylinder in the cavity closure stage as shown in Fig. 30. The downward point entry with three entry velocities all forms the complete cavity due to the vertical-up velocity of wave particle. In Fig. 31, the downward point entry with v = 0.5 m/s has a smaller complete cavity volume resulting in a greater cavity compression rate, which leads to the larger pressure on the cylinder top surface.

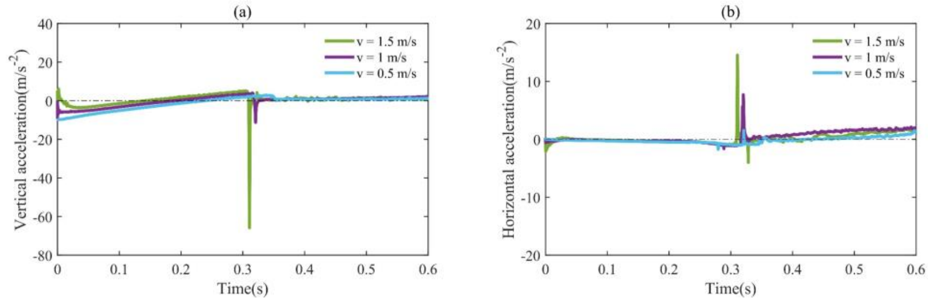

Fig. 28 Comparison of accelerations of the cylinder with different initial velocities in the wave upward position: (a) vertical acceleration; (b) horizontal acceleration.

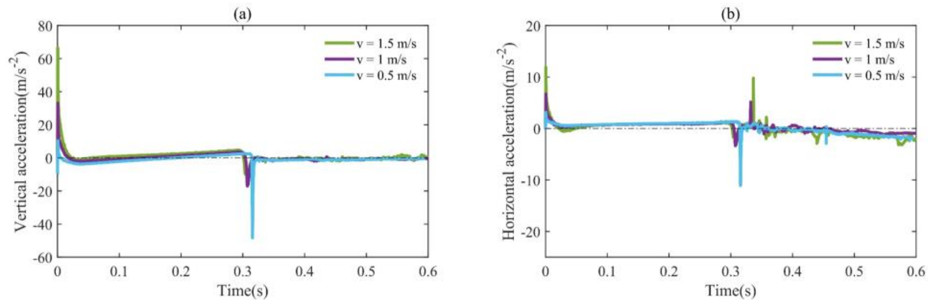

Fig. 29 Comparison of accelerations of the cylinder with different initial velocities in the wave downward point: (a) vertical acceleration; (b) horizontal acceleration.

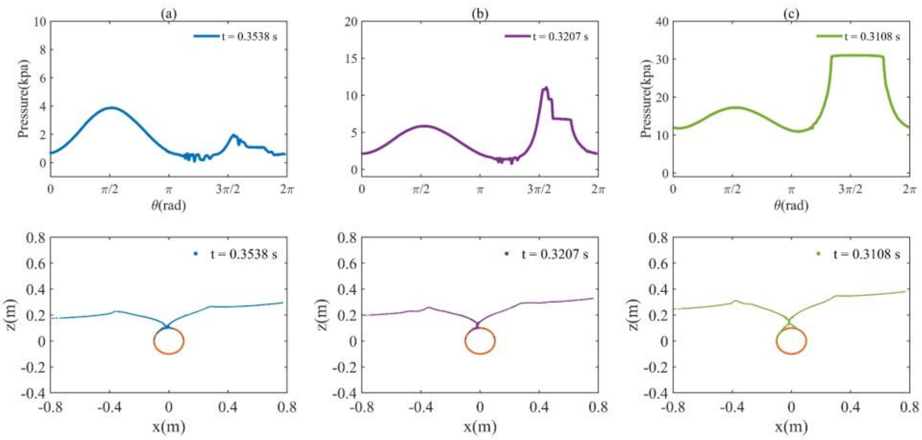

Fig. 30 Pressure distribution and free surface profile in the upward point entry at the moment of cavity closure: (a) v = 0.5 m/s; (b) v = 1.0 m/s; (c) v = 1.5 m/s.

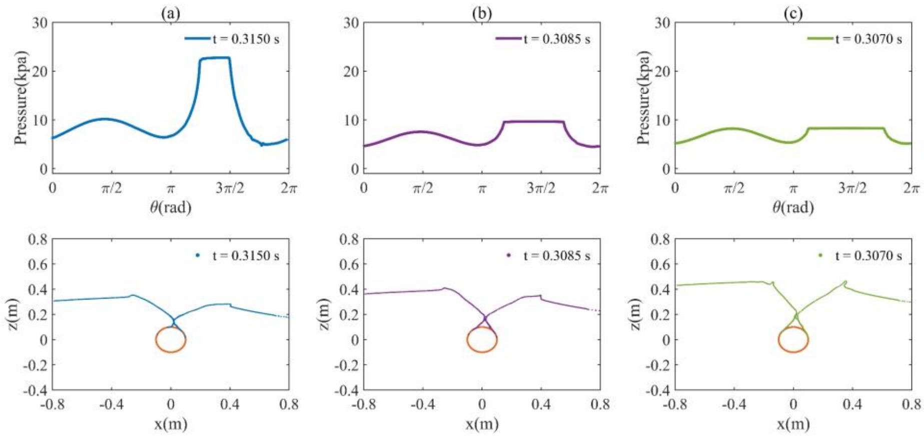

Fig. 31 Pressure distribution and free surface profile in the downward point entry at the moment of cavity closure: (a) v = 0.5 m/s; (b) v = 1.0 m/s; (c) v = 1.5 m/s.

At the moment of cavity closure, the vertical velocity of a cylinder with different entry positions is presented in Fig. 32. In each entry position case, the vertical velocity of the cylinder is similar in the cavity close stage which is almost independent of the initial impact velocity. This is because the cylinder with a larger entry velocity is subjected to larger hydrodynamic forces resulting in a faster deceleration of the cylinder. It also can be found that the vertical velocity in the cavity closure stage for the crest and upward point entries is larger than that for the trough and downward point entries.

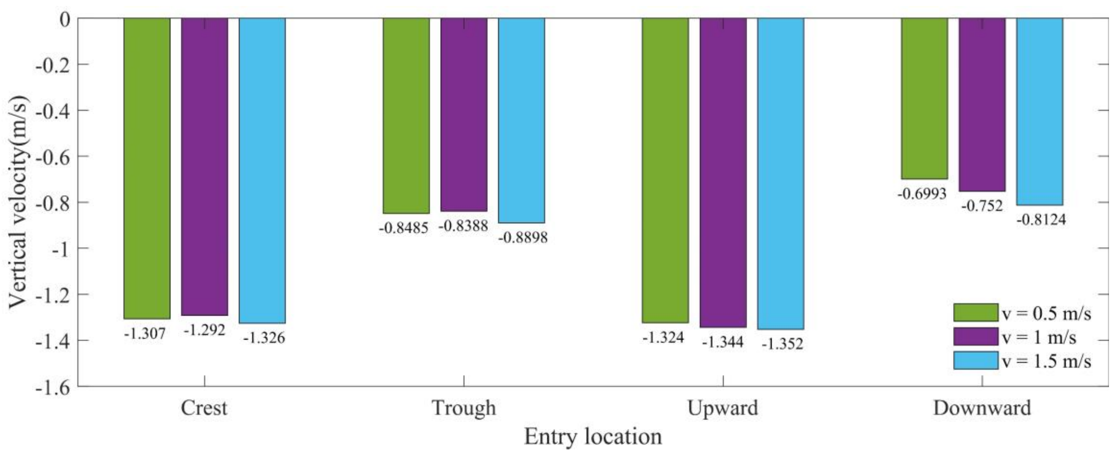

Fig. 32 Vertical velocity of the cylinder at the moment of cavity closure.

5. Conclusion

This paper investigates numerically the entire process of a cylinder entering the wave with the air cavity effect using the OpenFOAM. A convergence study for the jet profile of the cylinder entering the calm water is first performed to find an appropriate mesh scheme. By proposing the constraint for the *sixDoFRigidBodyMotion* solver, the process of the cylinder being lowered by a crane in the air, and then free-falling into the wave is simulated. Several case studies are conducted to further investigate the effects of the entry position and entry velocity on the wave entry of a cylinder. The following conclusions can be drawn based on the numerical results.

(1) The process of the cylinder entering waves can be divided into four stages, i.e. impacting stage, jet formation stage, cavity closure stage, and sinking stage according to the acceleration of the cylinder. At the beginning of impacting stage, the maximum pressure occurs in the jet root region which is the same as the pressure distribution of the wedge entry. Then the maximum pressure moves towards the centre of the bottom surface of the cylinder. During the jet formation stage, the jet separates from the cylinder surface, and the pressure and the vertical force gradually increase with the penetration depth. In the cavity closure stage, the jet roots on the left and right sides move toward each other to form a cavity. Then the cavity compressed by the liquid exerts a large pressure on the upper surface of the cylinder. In the sinking stage, the pressure on the left and right sides is more asymmetric with the penetration depth leading to an increase in the horizontal force.

(2) The effect of entry position on the cylinder entering waves can be summarized by two factors, i.e., the wave particle velocity and the wave slope. At the wave crest and trough positions,

the horizontal velocity of the wave particle contributes to the asymmetric effect on the pressure distribution. Because the horizontal velocity decays more rapidly along with the depth, the asymmetric pressure distribution gradually disappears as the cylinder moves down. The wave slope at the upward and downward points causes pressure asymmetry on both sides of the cylinder.

(3) The effect of the water entry velocity is mainly reflected in the impacting stage and cavity closure stage. A larger water entry velocity causes greater slamming pressure on the cylinder bottom surface in the impacting stage. Then the cavity volume is positively related to the effective entry velocity. When the effective entry velocity is small, the cavity formation is incomplete leading to the small pressure on the cylinder top surface at the moment of cavity closure. When the effective entry velocity is large enough to form a complete cavity, the pressure at the top of the cylinder is negatively related to the effective entry velocity. Moreover, the cylinder velocity at the moment of cavity close is almost independent of the initial impact velocity for each entry position.

The research in this paper provides guidance for the design of controllers for hoisting payloads into the waves by the cranes in terms of the entry velocity, entry position, etc. However, this study still has some limitations. Firstly, the two-dimensional simulation can not obtain the three-dimensional characteristics of the water entry process. Second, the present work considers the water entry of a cylinder into regular waves which has a large gap with the real complex sea state. Finally, the effect of the crane cable on the water entry is ignored, which is different from real crane operations. We would try to break through the limitations in our future research.

Acknowledgments

This work is supported by the Key Research and Development Project of Shandong Province under Grant 2021CXGC010701 and the National Natural Science

Foundation of China-Shandong Province under Grant U1706228.

References

Aliyar, S., Ducrozet, G., Bouscasse, B., Bonnefoy, F., Sriram, V., Ferrant, P., 2022. Numerical coupling strategy using HOS-OpenFOAM-MoorDyn for OC3 Hywind SPAR type platform. Ocean Eng. 263, 112206. https://doi.org/10.1016/j.oceaneng.2022.112206.

Bao, C.M., Wu, G.X., Xu, G., 2017. Simulation of freefall water entry of a finite wedge with flow detachment. Appl. Ocean Res. 65, 262-278. https://doi.org/10.1016/j.apor.2017.04.014.

Bouscasse, B., Colagrossi, A., Marrone, S., Antuono, M., 2013. Nonlinear water wave interaction with floating bodies in SPH. J. Fluids Struct. 42, 112-129. https://doi.org/10.1016/j.jfluidstructs.2013.05.010.

Chen, C.W., Wang, T., Feng, Z., Lu, Y., Huang, H., Ji, D., Chen, Y., 2020. Simulation research on water-entry impact force of an autonomous underwater helicopter. J. Mar. Sci. Technol. 25 (4), 1166-1181. https://doi.org/10.1007/s00773-020-00707-8.

Chen, H., Qian, L., Ma, Z., Bai, W., Li, Y., Causon, D., Mingham, C., 2019. Application of an overset mesh based numerical wave tank for modelling realistic free-surface hydrodynamic problems. Ocean Eng. 176, 97-117. https://doi.org/10.1016/j.oceaneng.2019.02.001.

Chen, J., Xiao, T., Wu, B., Wang, F., Tong, M., 2022. Numerical study of wave effect on water entry of a three-dimensional symmetric wedge. Ocean Eng. 250, 110800. https://doi.org/10.1016/j.oceaneng.2022.110800.

Chen, L., Zang, J., Hillis, A., Morgan, G., Plummer, A., 2014. Numerical investigation of wave–structure interaction using OpenFOAM. Ocean Eng. 88, 91-109. https://doi.org/10.1016/j.oceaneng.2014.06.003.

Cheng, Y., Ji, C., Zhai, G., Oleg, G., 2018. Numerical investigation of water entry of a wedge into waves with current effects using a fully nonlinear HOBEM. Ocean Eng. 153, 33-52. https://doi.org/10.1016/j.oceaneng.2018.01.092.

Cheng, Y., Yuan, D., Ji, C., 2021. Water entry of a floating body into waves with air cavity effect. J. Fluids Struct. 104, 103302. https://doi.org/10.1016/j.jfluidstructs.2021.103302.

Cheng, Y., Yuan, D., Ji, C., Li, G., 2019. Solitary wave slamming induced by an asymmetric wedge through three degrees of freedom free motions. Phys. Fluids 31 (097103), 1–21. https://doi.org/10.1063/1.5119443.

Cointe, R., Armand, J.L., 1987. Hydrodynamic Impact Analysis of a Cylinder. J. Offshore Mech. Arct. Eng. 109 (3), 237-243. https://doi.org/10.1115/1.3257015.

Derakhshanian, M.S., Haghdel, M., Alishahi, M.M., Haghdel, A., 2018. Experimental and numerical investigation for a reliable simulation tool for oblique water entry problems. Ocean Eng. 160, 231-243. https://doi.org/10.1016/j.oceaneng.2018.04.080.

Dobrovol'skaya, Z.N., 1969. On some problems of similarity flow of fluid with a free surface. J. Fluid Mech. 36 (4), 805-829. https://doi.org/10.1017/S0022112069001996.

Ferro, P., Landel, P., Pescheux, M., Guillot, S., 2022. Development of a free surface flow solver using the Ghost Fluid Method on OpenFOAM. Ocean Eng. 253, 111236. https://doi.org/10.1016/j.oceaneng.2022.111236.

Greenhow, M., Lin, W.M., 1983. Nonlinear-free surface effects: experiments and theory. Department of Ocean Engineering, Massachusetts Institute of Technology, Cambridge.

Howison, S.D., Ockendon, J.R., Wilson, S.K., 1991. Incompressible water-entry problems at small deadrise angles. J. Fluid Mech. 222, 215-230. https://doi.org/10.1017/S0022112091001076.

Jiang, C.X., Shuai, Z.J., Zhang, X.Y., Li, W.Y., Li, F.C., 2016. Numerical study on the transient behavior of water-entry supercavitating flow around a cylindrical projectile influenced by turbulent drag-reducing additives. Appl. Therm. Eng. 104, 450-460. https://doi.org/10.1016/j.applthermaleng.2016.05.102.

Korobkin, A., Guéret, R., Malenica, Š., 2006. Hydroelastic coupling of beam finite element model with Wagner theory of water impact. J. Fluids Struct. 22 (4), 493-504. https://doi.org/10.1016/j.jfluidstructs.2006.01.001.

Larsen, E., 2013. Impact loads on circular cylinders. Inst. Mar. Tek.

Lin, Y., Ma, N., Gu, X., 2021. Potential-flow and CFD investigations of bow-flare slamming on a container ship in regular heading waves. Ocean Eng. 219, 108278. https://doi.org/10.1016/j.oceaneng.2020.108278.

Ma, Z.H., Qian, L., Martínez-Ferrer, P.J., Causon, D.M., Mingham, C.G., Bai, W., 2018. An overset mesh based multiphase flow solver for water entry problems. Comput. Fluids 172, 689-705. https://doi.org/10.1016/j.compfluid.2018.01.025.

Schäffer, H.A., Klopman, G., 2000. Review of multidirectional active wave absorption methods. J. Waterw. Port Coast. Ocean Eng. 126 (2), 88-97. https://doi.org/10.1061/(ASCE)0733-950X(2000)126:2(88).

Semenov, Y.A., Iafrati, A., 2006. On the nonlinear water entry problem of asymmetric wedges. J. Fluid Mech. 547, 231-256. https://doi.org/10.1017/S0022112005007329.

Skjelbreia, L., Hendrickson, J., 1960. Fifth order gravity wave theory. Coast. Eng. Proc. 1 (7), 10-10.

Sun, P., Zhang, A.M., Marrone, S., Ming, F., 2018. An accurate and efficient SPH modeling of the water entry of circular cylinders. Appl. Ocean Res. 72, 60-75. https://doi.org/10.1016/j.apor.2018.01.004.

Sun, S.Y., Sun, S.L., Wu, G.X., 2015. Oblique water entry of a wedge into waves with gravity effect. J. Fluids Struct. 52, 49-64. https://doi.org/10.1016/j.jfluidstructs.2014.09.011.

Sun, S.Y., Wu, G.X., Xu, G., 2019. Free fall motion of a floating body: Bubble formation and its effect. Eur. J. Mech. B Fluids 76, 178-189. https://doi.org/10.1016/j.euromechflu.2019.02.009.

Von Karman, T., 1929. The impact on seaplane floats during landing. NACA Tech Note 321.

Wagner, H., 1932. Phenomena associated with impacts and sliding on liquid surfaces. J. Appl. Math. Mech. 12 (4), 193–215.

Wang, J., Lugni, C., Faltinsen, O.M., 2015. Experimental and numerical investigation of a freefall wedge vertically entering the water surface. Appl. Ocean Res. 51, 181-203. https://doi.org/10.1016/j.apor.2015.04.003.

Wang, K., Ma, X., Bai, W., Lin, Z., Li, Y., 2021. Numerical simulation of water entry of a symmetric/asymmetric wedge into waves using OpenFOAM. Ocean Eng. 227, 108923. https://doi.org/10.1016/j.oceaneng.2021.108923.

Wu, G.X., Sun, H., He, Y.S., 2004. Numerical simulation and experimental study of water entry of a wedge in free fall motion. J. Fluids Struct. 19 (3), 277-289. https://doi.org/10.1016/j.jfluidstructs.2004.01.001.

Xiang, G., Soares, C.G., 2020. Improved dynamical modelling of freely falling underwater cylinder based on CFD. Ocean Eng. 211, 107538. https://doi.org/10.1016/j.oceaneng.2020.107538.

Xiang, G., Wang, S., Guedes Soares, C., 2020. Study on the motion of a freely falling horizontal cylinder into water using OpenFOAM. Ocean Eng. 196, 106811.

https://doi.org/10.1016/j.oceaneng.2019.106811.

Xu, G.D., Duan, W.Y., Wu, G.X., 2008. Numerical simulation of oblique water entry of an asymmetrical wedge. Ocean Eng. 35 (16), 1597-1603. https://doi.org/10.1016/j.oceaneng.2008.08.002.

Xu, G.D., Duan, W.Y., Wu, G.X., 2010. Simulation of water entry of a wedge through free fall in three degrees of freedom. Proc. R. Soc. A. 466 (2120), 2219–2239. https://doi.org/10.1098/rspa.2009.0614.

Zhao, R., Faltinsen, O., 1993. Water entry of two-dimensional bodies. J. Fluid Mech. 246, 593–612. https://doi.org/10.1017/S002211209300028X.